Numerical simulation of the tunneling current and ballistic electron effects in field emission devices

L. R. C. Fonseca,[a] Paul von Allmen, and R. Ramprasad
Motorola, Inc., Flat Panel Display Division, 7700 South River Parkway, FPD22, Tempe, Arizona 85284

(Received 13 September 1999; accepted for publication 9 November 1999)

Using a two-dimensional model, we have considered the effects of spatially changing fields and potentials, stochastic electron emission, and ballistic electron motion on the anode current and on the width of the electron beam in field emission displays. We have solved the electrostatic problem using the boundary element method. Our electron emission model evaluates the current density at the cathode surface from the tunneling transmission coefficient, which is calculated from the solution of the one-dimensional Schrödinger equation using a potential barrier which includes the effect of image charges and nonuniform electric field. The current density is used to calculate the rate of electron emission for each segment of the emitter's surface. The emission time is assumed to follow a Poisson distribution. The electron's velocity magnitude and angle with the normal to the surface are also stochastically generated following the probability distribution of field emitted electrons. Ballistic transport is used to propagate electrons through the device. For very sharp tips the electric field changes from its surface value over a very short distance away from the surface, which can be comparable to the tunneling distance. We found that the resulting current density is considerably lower for the calculated barrier profile than for the triangular one, especially at low values of the electric field. We have also shown that the effect of the lateral kinetic energy and emission angle distribution on the electron beam width at the anode is negligible for sharp emitters, where the angular spread is dominated by the curvature of the emitting surface. © *2000 American Institute of Physics.* [S0021-8979(00)05104-5]

I. INTRODUCTION

Field emission devices (FEDs) pose a considerable challenge for numerical simulations due to the many length scales present in the system, typically spanning more than six orders of magnitude. For instance, electron emission occurs at the tip of small metallic cones or at the cap of carbon nanotubes, with dimensions of the order of 100 Å for the former and 10 Å for the latter, while typical anode-cathode distances can be of the order of hundreds of microns.

In this article we describe an algorithm to model complete FEDs, from the electron tunneling scale to macroscopic device elements. We illustrate the method with two applications: the effect of spatial changes of the electric field on the emitted current density and the effect of the emission angle on the spread of the electron beam.

To accurately calculate the electric field in a FED we have chosen the boundary element method (BEM).[1,2] BEM consists in writing the Poisson equation in terms of surface integrals using Green's function techniques and discretizing the boundaries to solve the integrals numerically. In three-dimensions (3D) the BEM converts the 3D differential equation to a 2D surface integral equation, while in 2D, it converts the 2D differential equation to a line integral. In both cases, the number of independent variables is decreased by one, facilitating the numerical solution of the multiscale problem. BEM also handles irregular domains very well. As described in detail in the next section, using the BEM one can obtain the values of the electric field and potential at every point of the domain. However, BEM is not very efficient if the values of the electric field or potential are needed over a very large number of points, e.g., if the field values are needed over a fine discretization grid.

Because of the exponential nature of the emitted current, the performance of FEDs is strongly dependent on system parameters. Thus, it is necessary to consider a detailed description of the emission process. Our emission model consists of stochastic field emission, where the emission parameters, namely emission velocity magnitude, emission angle with the normal to the surface, and emission time are determined from the probability distribution of field emitted electrons at the surface of the cathode. Such a probability distribution is the product of the supply function and the transmission coefficient through the tunnel barrier, which includes image charge effects as well as spatial variations of the electric field near the tip. Once emitted, electrons are propagated across the device using ballistic transport.

The resulting algorithm, based on a 2D model of field emission, is very general, efficient, and easy to use. We have applied it to different problems, from cathode design optimization to charging of device elements resulting from electron hits.

Despite the quantitative limitations imposed by the lower dimensionality of our model, the qualitative results we obtained offer useful insights. The limitation of a 2D model is mostly in the field enhancement factor, not in the emission process. In other words, given the electric field along the surface of the emitter, the value of the 2D and 3D currents

[a]Electronic mail: l.fonseca@motorola.com

for realistic emitter dimensions differ by approximately one order of magnitude. Because of the exponential nature of the emitted current, small uncertainties on system parameters will lead to changes in the current of more than one order of magnitude. Thus, the disagreement between the 2D and 3D currents is in the uncertainty range of the system parameters.

In Sec. II we describe the BEM, the stochastic electron emission, and the electron transport across the device. In Sec. III we illustrate the algorithm by comparing current densities obtained with calculated and triangular tunnel barriers. We also discuss the effect of the electron emission angle on the spread of the electron beam.

II. METHOD

A. Solution of the electrostatic problem: The BEM

The BEM can be used to solve the general electrostatic problem where charges are present in the system. For simplicity, we will only consider the case where there is no accumulation of charges anywhere in the device and where the emitted current is low enough that space charge effects are not important. The latter approximation holds for emitters operating in the range of currents less than $\sim 1\,\mu$A, which is typical for metallic FED cathodes. The formal extension of the method to the general case is straightforward.

The 2D chargeless electrostatic problem is described by the Laplace equation on which Dirichlet boundary conditions are imposed

$$(\partial_{xx}^2+\partial_{yy}^2)\Phi(\mathbf{r})=0, \quad \Phi(\Gamma)=\Phi_0(\mathbf{r}), \tag{1}$$

where Γ is the perimeter of the integration domain S and $\Phi_0(\mathbf{r})$ is the potential at the boundaries. Using Green's theorem, the earlier differential equation can be written as an integral equation

$$\Phi(\mathbf{r})=\oint_\Gamma [G(\mathbf{r},\mathbf{r}')\nabla_n'\Phi(\mathbf{r}')-\Phi(\mathbf{r}')\nabla_n' G(\mathbf{r},\mathbf{r}')]dr', \tag{2}$$

where the derivatives are taken along $\mathbf{n}$, the normal to the contour and directed outwards, and the Green's function $G(\mathbf{r},\mathbf{r}')$ is defined by

$$(\partial_{xx}^2+\partial_{yy}^2)G(\mathbf{r},\mathbf{r}')=\delta(\mathbf{r}-\mathbf{r}'). \tag{3}$$

In 2D the Green's function is given by the following expression:

$$G(\mathbf{r},\mathbf{r}')=-\frac{1}{2\pi}\ln|\mathbf{r}-\mathbf{r}'|. \tag{4}$$

If $\mathbf{r}$ is taken on Γ, Eq. (2) determines the electric field $F=-\nabla_n\Phi$ on Γ, normal to the contour.

The numerical expression for Eq. (2) is obtained by dividing the contour Γ into L segments $\Gamma_j=[\mathbf{r}_j,\mathbf{r}_{j+1}]$, $j=1,\ldots,L$, which transforms the integral equation into an algebraic equation

$$\Phi_i=-\sum_{j=1}^{L}(G_{ij}F_j+G_{ij}'\Phi_j), \tag{5}$$

where

$$\Phi_i=\Phi(\mathbf{r}_i),$$

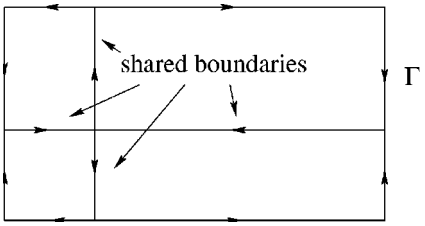

FIG. 1. Schematic representation of a domain boundary Γ and shared subdomain boundaries. The arrows along the boundaries show one of the two possible line integration directions.

$$F_j=-\nabla_n\Phi(\bar{\mathbf{r}}_j),$$

$$G_{ij}=\int_{\Gamma_j}G(\mathbf{r}_i,\mathbf{r})dr, \tag{6}$$

$$G_{ij}'=\int_{\Gamma_j}\nabla_n G(\mathbf{r}_i,\mathbf{r})dr,$$

$$\bar{\mathbf{r}}_j=\frac{\mathbf{r}_j+\mathbf{r}_{j+1}}{2},$$

$\mathbf{r}_i=$ interior point.

The index i labels any point of the domain, while j labels points on Γ. To evaluate Φ_i in Eq. (5) the value of the electric field along the boundary, F_j, is needed. By taking $r_i \in \Gamma$, F_j is given in matrix notation by

$$F=-G^{-1}(G'+1)\Phi_0. \tag{7}$$

So far we have assumed a position-independent dielectric constant. If the domain is composed of many subdomains S_i, each one characterized by a position-independent dielectric constant ϵ_i, then we have an equation like Eq. (2) for each subdomain (see Appendix A). However, in this case, Φ_i is not known at every point along the boundaries, since some boundaries are shared between subdomains (see Fig. 1). The additional unknowns added to the problem are balanced by the use of the continuity of the normal component of the electric displacement field across neutral interfaces: $\epsilon_l^k F_l^k=\epsilon_r^k F_r^k$, where l/r corresponds to the left/right sides of the shared boundary k.

Once the electric field is calculated using Eq. (7), the determination of the potential at nonboundary points involves a single summation over the boundary elements, given by Eq. (2), while the electric field at nonboundary points is given by similar expressions ($F=-\nabla\Phi$). This is a major advantage of the BEM over grid methods like finite differences or finite elements: the potential and electric field can be calculated at any point of space by performing a simple summation, which is insensitive to the relative magnitude of the terms in the sum (as long as proper computer precision is used). On the contrary, in finite elements or finite differences, the values of the electric field and potential on the grid are obtained from a matrix inversion, an operation that imposes restrictions on the relative magnitude of the matrix elements. For a multiscale problem like the simulation of FEDs, such restrictions result in grids with a very large number of points, leading to large storage require-

ments. On the other hand, even though a summation over boundary elements is computationally fast, if the potential and/or the electric field are needed at a large number of points, then the time spent to perform each summation times the number of points may be large. In this case, grid methods may be advantageous, because the matrix is inverted only once, and the value of the field at any point can be obtained by simple interpolation. In the case of FED simulations, the electric field and potential are only needed within the electronic beam, which fills only a small portion of the whole device, and therefore the BEM is the method of choice.

B. Electron emission

In order to emit an electron from a point at the emitter surface we generate the following three random numbers: the emission time t, the velocity component normal to the surface and the velocity component parallel to the surface, v_x and v_y respectively, at the emission location. We use the probability distribution of field emitted electrons $N(v_x,v_y)$ to determine these random numbers

$$N(v_x,v_y)=\frac{N_0}{(2\pi)^2}\left(\frac{m}{\hbar}\right)^2 v_x F(v)T(v_x), \tag{8}$$

where m is the free electron mass, N_0 is the normalization factor, $v=(v_x^2+v_y^2)^{1/2}$, T is the transmission coefficient, and F is the Fermi function

$$F(v)=\frac{1}{1+\exp[\beta(E(v)-\mu)]}, \quad E(v)=\tfrac{1}{2}mv^2. \tag{9}$$

In Eq. (9), μ is the chemical potential, $\beta=(k\tau)^{-1}$, τ is the temperature, and $E(v)$ is the electron's classical kinetic energy. The transmission coefficient T is obtained from the open boundary solution of the Schrödinger equation for a given potential $V(\mathbf{r})$. In order to avoid solving the full 2D scattering problem[3] (see discussion later), we have assumed that the emitted electrons tunnel through the barrier along the normal to the surface. In that case, the 2D potential $V(\mathbf{r})$ reduces to a 1D effective potential $V_{\text{eff}}(\xi)$, where ξ is the coordinate along the normal to each point of the surface and T is obtained from the solution of a 1D Schrödinger equation with the effective potential V_{eff} (see Appendix B).

The emission rate r_i from the ith boundary element is obtained from the corresponding surface current density j_i

$$r_i=\frac{\Delta l_i}{e}j_i, \tag{10}$$

where Δl_i is the length of the ith boundary element, and the current density per unit length is given by

$$j_i=e\int_0^\infty dv_x\int_{-\infty}^\infty dv_y N_i(v_x,v_y). \tag{11}$$

Using the emission rate, we determine the emission time of the nth electron from the ith boundary element following a Poisson distribution

$$t_i^n=t_i^{n-1}-\frac{1}{r_i}\log(1-\zeta), \tag{12}$$

where ζ is a uniformily distributed random number, $0<\zeta<1$.

The generation of the random velocity components for each electron emitted by each boundary element is complicated by the fact that $N(v_x,v_y)$ cannot be decomposed as a product of two distribution functions of the velocity components. For distribution functions with coupled random variables, the standard procedure, called rejection method[4] is the following: (1) generate a pair (v_x,v_y) using a distribution function $K(v_x,v_y)$ for which the directions can be decoupled, $K(v_x,v_y)=K_1(v_x)\times K_2(v_y)$, and such that $N(v_x,v_y)/K(v_x,v_y)\leqslant 1$; (2) use $N(v_x,v_y)$ to reject or accept the pair (v_x,v_y): accept it if $N(v_x,v_y)/K(v_x,v_y)>\zeta$, reject it otherwise. As earlier, ζ is a uniformily distributed random number. In step (1) we have chosen a normal distribution for K and adjusted the mean velocity $\overline{v_x}$ and variances σ_x and σ_y to best fit $N(v_x,v_y)$ (the mean velocity parallel to the emission plane is zero). We then multiplied K by a constant A such that $A\times K>N$ for all (v_x,v_y) pairs. The number of rejections is of the order of the area under $A\times K$ (since N is normalized) and is typically less than 100.

The normally distributed velocity components are then given by

$$\begin{aligned} v_x&=\sqrt{-2\log(\zeta_x)}\sin\left(\frac{\zeta_y}{\sigma_x\sigma_y A}\right)\sigma_x+\overline{v_x},\\ v_y&=\sqrt{-2\log(\zeta_x)}\cos\left(\frac{\zeta_y}{\sigma_x\sigma_y A}\right)\sigma_y, \end{aligned} \tag{13}$$

where ζ_x and ζ_y are uniformily distributed random numbers. After the velocity vector $\mathbf{v}=(v_x,v_y)$ is generated and accepted in the local reference frame of the boundary element, it is rotated to the reference frame of the device. Thus, for an emitter shaped as half a circle for example, the velocity of an electron emitted at the apex remains unchanged under a rotation, but velocities for emission from all other locations are rotated. Consequently, even if $v_x=0$ (emission perpendicular to the surface), the electron's lateral velocity may still be nonzero in the device reference frame.

C. Electron propagation

Electrons are propagated ballistically through the device following Newton's equation of motion. We use the Verlet algorithm to calculate each electron's position and velocity

$$\begin{aligned} r_i^n&=r_{i-1}^n+\frac{1}{2}\frac{eF_{i-1}}{m}\delta t_{i-1}^n(\delta t_{i-1}^n+\delta t_{i-2}^n)+\frac{\delta t_{i-1}^n}{\delta t_{i-2}^n}\\ &\quad\times(r_{i-1}^n-r_{i-2}^n),\\ v_{i-1}^n&=\frac{r_i^n-r_{i-2}^n}{\delta t_{i-1}^n+\delta t_{i-2}^n}-\frac{1}{2}\frac{eF_{i-1}}{m}(\delta t_{i-1}^n-\delta t_{i-2}^n), \end{aligned} \tag{14}$$

where the indices i and n refer to step number and electron number, respectively, and $F_i\equiv F(r_i)$ is the electric field. Notice that the velocity is one step ''late'' with respect to the location. Because the Verlet algorithm requires knowledge of the two prior positions, a second-order accurate expression for the first step is used

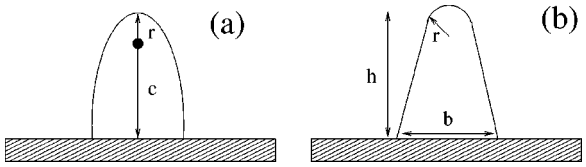

FIG. 2. (a) Schematic representation of the cross section of an elliptical cone and elliptical cylinder. The first is obtained by rotating the cross section around the major axis, while the latter is obtained by a rigid translation of the cross section. (b) Geometry used in our numerical calculations.

$$r_1^n = r_0 + \delta t_0 v_0^n + \frac{1}{2}\frac{eF(r_0^n)}{m}\delta t_0^2, \tag{15}$$

where δt_0 is a small time step. In order to accelerate the calculations we have implemented a scheme in which each electron is propagated according to its own time step. For example, if electron A is propagated over a time step δt and electron B is propagated over a time step $\delta t/k$, then for the next $k-1$ steps of electron B, electron A is not propagated. This scheme is very helpful if there are several electrons being simultaneously propagated in the device. The step length is short or long depending whether the electric field is quickly or slowly varying at the electron location

$$\delta t_i = \frac{1}{v_{i-1}}\sqrt{\frac{2\kappa}{M}\frac{|r_i - r_{i-1}|}{|F_i - F_{i-1}|}}, \tag{16}$$

where M is the minimum number of steps required to reach the anode. The earlier relation is derived by assuming conservation of energy within a total error tolerance κ.

III. APPLICATIONS

A. Comparison between 2D and 3D models

Before discussing trends provided by our 2D model, we will evaluate to what extent the 2D model gives valuable insight when studying a 3D system. We first compare the field enhancement factor for needle-like structures such as cones with that for wedge-like structures. To illustrate the difference, let us consider two geometries with known analytical expressions for the field enhancement factor: the elliptical cone and the elliptical cylinder. The elliptical cone is obtained by rotating the cross section of Fig. 2(a) around the ellipse's major axis, while the elliptical cylinder is obtained by translating the same cross section between $-\infty$ and $+\infty$. Let us define the field enhancement factor M as

$$M = \frac{F}{F_0}, \tag{17}$$

where F is the electric field at the apex of the tip, while F_0 is the electric field far from the tip. The field enhancement for the elliptical cone, M_{cone}, and elliptical cylinder, M_{cyl}, are[5]

$$M_{\text{cone}} \approx \frac{2\frac{c}{r}}{\ln\left(4\frac{c}{r}\right) - 2},$$

$$M_{\text{cyl}} = \left(1 + \sqrt{\frac{c}{r}}\right), \tag{18}$$

where r and c are the ellipse's focus-to-apex and major axis, respectively. For a radius $r = 100$ Å and a tip height $c = 1$ μm we obtain $R = M_{\text{cone}}/M_{\text{cyl}} \approx 3.3$. Because the current emitted depends exponentially on the electric field, such a ratio implies current densities many orders of magnitude lower for the elliptical cylinder than for the elliptical cone for a fixed voltage bias. If the quantity of interest in a 2D simulation of a 3D device containing an elliptical cone is the current, then one has to scale the voltage bias by approximately R (in a diode configuration the scaling is exactly R while for the triode configuration the scaling is only approximate since there are two voltage sources and only one is scaled). If the quantity of interest in the simulation is the trajectory of the electrons, then we recommend to use realistic voltage bias and, hence, low currents. Indeed, the electron trajectories obtained from a simulation with scaled bias voltage depend on the device geometry and can lead to erroneous interpretations: in the diode mode the cone of emission will be narrower than it should since under a higher *anode* voltage bias the electrons spend less time in the device and thus propagate less in the lateral direction. On the contrary, in the triode mode the beam will be wider, since a higher *gate* voltage more strongly pulls the electrons laterally towards the gates.

The second difference between a 2D and a 3D simulation is the current emitted given the field at the surface. We derived the 2D Fowler–Nordheim (F–N) current density assuming low temperature, no image charge, and a triangular barrier

$$j_{2D}(F,w) = 1.017\times 10^3 \left(\frac{F^2}{w}\right)^{3/4} \exp\left(-0.683\frac{w^{3/2}}{F}\right)\frac{A}{\text{cm}}, \tag{19}$$

where F is the electric field in V/Å and w is the work function in electron volts. Comparing the earlier expression with the usual 3D F–N[6]

$$j_{3D}(F,w) = 1.537\times 10^{10}\frac{F^2}{w}\exp\left(-0.683\frac{w^{3/2}}{F}\right)\frac{A}{\text{cm}^2}, \tag{20}$$

one obtains, for a typical electric field $F = 3\times 10^{-1}$ V/Å and work function $w = 4.5$ eV, a current density ratio $j_{3D}/j_{2D} \approx 5\times 10^6$. If we assume a uniform semispherical/circular emitter geometry in 3D/2D, with emission radii $r = 100$ Å, we obtain a surface area of $6.3\times 10^{-12}\,\text{cm}^2$ and a surface length of $3.1\times 10^{-6}\,\text{cm}$, and a current ratio $I_{3D}/I_{2D} \approx 10$. Thus, while the field enhancement obtained in 2D is considerably smaller than in the 3D case, the current emitted by a segment of realistic length in 2D is quite close to the 3D current emitted by an equivalent area.

B. Realistic versus triangular barriers

Because sharp tips display such strong field enhancement, the electric field in the region of the tip can change by a considerable fraction over a distance comparable to the tunneling length. The resulting nontriangular barrier has been discussed by several workers.[7–9] The exact description

TABLE I. Electric field and current density at the surface of a triangular-shaped emitter with a circular cap as a function of the angle from the apex. Cap radius $r=100$ Å. Here and later, the triangle base length $b=0.5$ μm and the triangle height $h=1$ μm.

Angle (°)	0	15	30
Electric field (V/μm)	2.5×10^{3}	2.3×10^{3}	2.0×10^{3}
Current density (A/μm)	3.0×10^{-11}	8.2×10^{-12}	5.3×10^{-14}

of electron tunneling to vaccum from a sharp tip in a strong electric field requires a rather complex formalism, the solution of the full 3D scattering problem, which reduces to a 2D scattering problem in systems with azimuthal symmetry.[3,10] Since the systems of interest are emitter tips containing hundreds of atoms along their emissive area, we do not believe that such level of accuracy is needed. Indeed, the uncertainty in the tip radius, tip geometry, surface composition (presence or not of chemisorbed or physisorbed impurities), and surface temperature possibly play a larger role in realistic field emission structures than a more accurate treatment of the scattering process. We have therefore simplified the solution of the 2D scattering problem, while capturing the essential physics of the tunneling process, using the following approximation: we have assumed that the tunneling path is a straight line perpendicular to the emitter surface, and calculated the potential profile along that line. Thus, we still solve the usual 1D Schrödinger equation for the transmission coefficient, but we take into account the changing potential profiles starting from different points along the surface of the emitter. Such an approximation underestimates the local current density, since the major contribution to the tunneling current follows the shortest path under the barrier, which is not necessarily a straight line normal to the surface of the emitter.[11] However, since most of the current comes from the area around the apex of the emitter where the field is largest and where the shortest tunneling path is almost straight, we believe that our approximation is accurate enough to provide reasonable current values. As an illustration of the highly nonlinear effect of the electric field on the current density, Table I shows the electric field and current density as a function of the angle from the apex for a triangle-shaped tip [Fig. 2(b)]. Notice how fast the current density decreases as the angle from the apex increases.

Figure 3 shows typical barrier profiles obtained from the calculation of the potential along the tunneling path starting from the tip apex, and for a triangular barrier, for which the electric field is assumed constant on the scale of the tunneling length, and is given by its value at the surface of the emitter (the apex, in this particular example). Figure 4 shows the current density along the circular cap of the triangle as a function of the tip radius for calculated and triangular barriers, both added to a $\frac{1}{4}x$ image charge potential. Notice that the ratio between the two current densities $\rho_{\mathrm{calc}}/\rho_{\mathrm{tri}}$ remains constant along the entire length of the cap, which extends approximately 40° from the apex. The inset shows the average current density at the cap as a function of tip radius for calculated and triangular barrier profiles. As expected from the general barrier profile shown in Fig. 3, the current density is overestimated in the case of triangular barriers and slowly approaches the calculated result as the tip radius increases. For example, for an applied field of 200 V/μm, $\rho_{\mathrm{tri}}/\rho_{\mathrm{calc}}$ drops from ≈5 for $r=50$ Å (average electric field in the tip $\overline{V}_{\mathrm{tip}}=1000$ V/μm) to ≈3 for $r=500$ Å ($\overline{V}_{\mathrm{tip}}=3000$ V/μm). In other words, the difference between the calculated and the triangular barrier results (both including image charge) is weakly dependent on the tip radius. This is because two competing effects take place when the tip radius is varied: for increasing radii the calculated tunneling barrier is better and better approximated by the triangular barrier, and they exactly overlap for the case of an infinite tip radius (flat surface). However, as the radius increases, the field enhancement factor decreases, leading to a decrease in the electric field at the surface of the emitter. As a result, the area under the barriers above the Fermi level increases, and so do

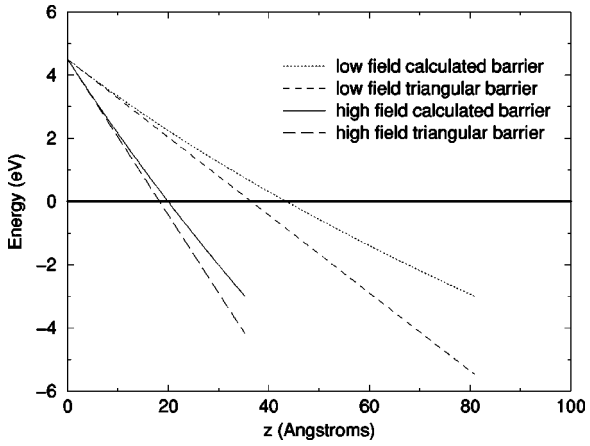

FIG. 3. Calculated potential barrier for low and high fields at the tip apex (solid—high field, dashed—low field) and assuming a triangular barrier shape (long dashed—high field, dotted—low field) where the constant electric field is given by its value at the surface (=2465 V/μm for high field and =1233 V/μm for low field). Thick solid line: Fermi level. Tip circular cap radius $r=100$ Å. Electric field far away from the tip: 200 V/μm. Work function $w=4.5$ eV.

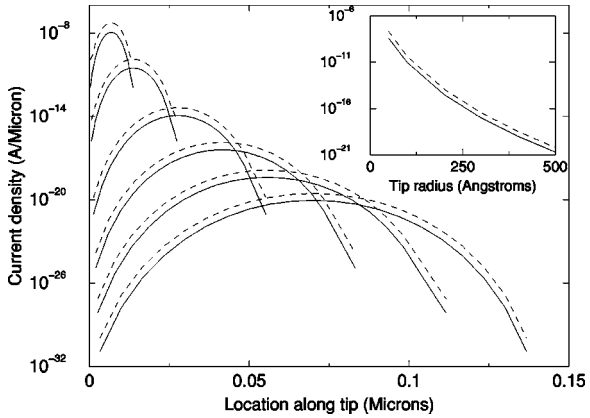

FIG. 4. Current density as a function of the location along the tip circular cap for calculated (solid) and triangular (dashed) barrier profiles, and for different tip radii ($r=50,100,200,300,400,500$ Å). Higher current density maximum corresponds to smaller tip radius. Inset: average current density at the cap as a function of tip radius for calculated (solid) and triangular (dashed) barrier profiles.

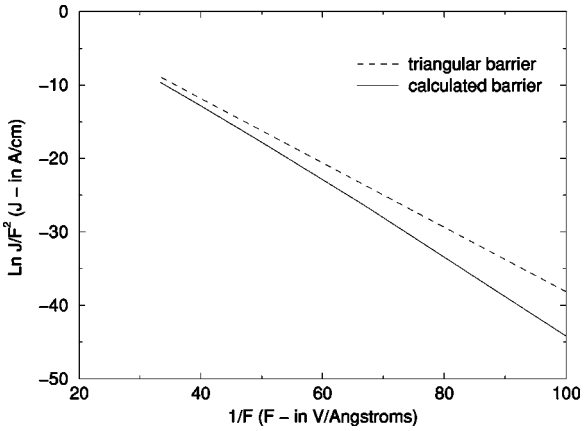

FIG. 5. F–N plot of the current density at the tip apex for calculated (solid) and triangular (dashed) barrier profiles, and for a tip radius $r=100$ Å. Image charge not considered.

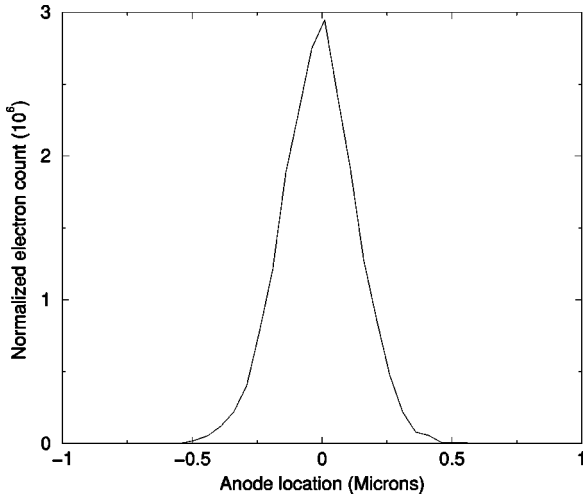

FIG. 6. Normalized count of electrons hitting the anode as a function of the location along the anode for a flat emitter. The center of the distribution is aligned with the emitter. Anode voltage $V_a=2\times10^4$ V, work function $w=2.5$ eV, tip radius $r=100$ Å, anode-cathode separation 100 μm.

the difference between the areas under the calculated and triangular barriers (see Fig. 3) and the ratio $\rho_{\text{tri}}/\rho_{\text{calc}}$.

Figure 5 shows the F–N plot of the current density at the tip apex for a fixed tip radius $r=100$ Å and for the two barrier profiles without image charge. We see now that $\rho_{\text{tri}}/\rho_{\text{calc}}$ rapidly decreases as the field increases. In this case, only the area under the barrier and above the Fermi level plays a role since the field enhancement is constant. Despite the fact that the surface electric field in this case is in the same range as for the case when the tip radius is varied (1000–3000 V/μm), $\rho_{\text{tri}}/\rho_{\text{calc}}$ now dropped from 350 to 2. Notice that the slope of the F–N plot for the calculated barrier approaches the slope for the triangular barrier at high fields. Therefore, in order to extract the field enhancement factor from the F–N plot for a nonplanar emitter, the slope at the high field extreme of the curve should be used. In the particular case shown in Fig. 5, knowing that the work function used is 4 eV, the field enhancement factor [Eq. (17)] obtained at high fields for the calculated barrier is 13.5, while the exact one is 12.3.

C. Effect of the emission angle on the spread of the electron beam

The solid angle of the cone of emission is determined by the combined effects of the curvature of the emitting surface and the lateral emission velocity of the electrons at each point of the surface. In the usual F–N approach the latter effect is eliminated through summation over all lateral velocities, which means that emission from a flat surface would produce a nondiverging electron beam at low currents (at very high currents, electron–electron repulsion would still lead to a divergent beam). The spread of the electron beam is also a function of the potential difference V_a between anode and cathode, because the lateral velocity remains close to its value at emission. The spread of the beam is therefore bigger for smaller values of V_a because electrons spend more time to cross the device which results in enhanced lateral propagation. We will now discuss the spread of the electron beam considering a typical device geometry and a typical V_a. Room temperature will be used in all cases.

Figure 6 shows the normalized electron distribution along the anode for an anode-cathode separation of 100 μm and potential difference $V_a=2\times10^4$ V. The cathode is assumed flat and electrons are emitted from a single point. We use a low work function, $w=2.5$ eV, to increase the emission rate for lower V_a. This configuration leads to a solid angle between the center of the peak and the peak half height of $\Omega\approx0.15°$ while the usual F–N procedure gives $\Omega=0$. Notice that in the diode configuration, V_a serves two purposes: to decrease the tunneling barrier for electron emission and to provide electrons with enough energy to excite the phosphor that coats the FED anode. Energies in the range 3×10^3–1×10^4 eV are typically needed for bright color displays.[12] Using a triode mode, the value of V_a can be decreased from 10^4 V, while lowering the tunneling barrier can be accomplished with the use of a gate structure close to the emitting surface. Also, in the case of monochrome displays or low voltage color phosphors, much lower energies and therefore V_a are needed (150–300 eV).[12] The spread $\Omega\approx0.15°$ can, hence, be considered as a lower bound for the solid emission angle from a flat surface since lower anode-cathode potential differences will result in considerably larger values of Ω. Also it should be noted that the electric field for gated structures has a lateral component leading to an additional spreading of the electronic beam.

Figure 7 shows the normalized electron distribution along the anode using the same parameters and device geometry as in the flat emitter case except that we use a triangular tip ($b=0.5, h=1$ μm, $r=100$ Å) in place of the flat emitter. Two situations were considered: emission with and without angular distribution, the latter case corresponding to emission perpendicular to the surface. For perpendicular emission the electrons hit the anode with a multipeak distribution, each peak corresponding to one of the discrete regions in the cathode with a nonzero electron distribution surface elements. The finite width of each peak is due to the fact that the emission velocity perpendicular to the surface is stochastic and contains a component along the anode-cathode

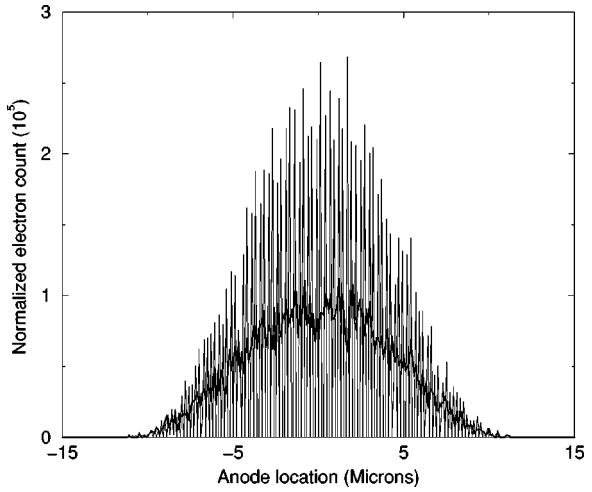

FIG. 7. Normalized counts of electrons hitting the anode as a function of the location along the anode for a tip emitter. The centers of the distributions are aligned with the emitter. Thin line: electron emission normal to the surface; thick line: electron emission including angular distribution. Anode voltage $V_a=2\times10^4$ V, work function $w=2.5$ eV, tip radius $r=100$ Å, tip height $h=1$ μm, tip width $b=0.5$ μm, anode-cathode separation 100 μm.

direction as well as a nonzero component perpendicular to it for emission from any location away from the tip apex. The multipeak nature of the distribution for perpendicular emission is an artifact of the numerical method but the total spread of the electron distributions is similar for the two cases. The reason is that the spread of the electron beam for the flat surface is of the order of 0.5 μm, while the spread due to the tip geometry is of the order of 10 μm. We can conclude from this calculation that the spread of the electron beam is mostly determined by the curvature of the emitter while the lateral velocity of the emitted electrons turns out to be a minor contribution.

IV. CONCLUSION

We have described an algorithmic approach to model field emission displays, capable of handling the many length scales present in these systems, ranging from the microscopic level, where tunneling and electron emission take place, to the macroscopic device scale. The model was developed in two dimensions, but can be readily expanded to three dimensions. We have analyzed the 2D model and concluded that, for realistic emitter dimensions, it underestimates the field enhancement by a factor of 3–4 and the emitted current by a factor of 10 if compared to a 3D system. We have illustrated the algorithm by calculating the difference between the current density for tunneling through triangular barriers and calculated barriers, the latter obtained from the numerical solution of Laplace equation. We have shown that the difference resulting from the two barrier profiles mostly occurs at small values of the electric field at the surface of the emitter, since at high fields the region where the two barriers differ is below the Fermi level where the emission current is low. We have also analyzed the effect of the angular velocity distribution on the spread of the electron beam and we have shown that the major contribution to the spread of the electron beam comes from the curvature of the emitting surface at the tip.

APPENDIX A

Given a system with N subdomains, the electrostatic potential within each subdomain can be written as follows:

$$\begin{aligned}
&\Phi_j^{(i)} = -\sum_{j'\in L_i}[G_{jj'}^{i} D_{j'}^{(i)} + G'^{(i)}_{jj'}\Phi_{j'}^{(i)}],\\
&D_j^{(i)} = -\epsilon_i \nabla_n \Phi_j^{(i)},\\
&G_{jj'}^{(i)} = \frac{1}{\epsilon_i}\int_{\Gamma_{j'}^{(i)}} dr G(r_j, r),\\
&G'^{(i)}_{jj'} = \int_{\Gamma_{j'}^{(i)}} dr \nabla_n G(r_j, r),\\
&L_i = E_i \bigcup_{i'=1;i'\neq i}^{N} S_{ii'},
\end{aligned} \tag{A1}$$

where L_i is the set of points on the boundary of domain i and is the union of the set of points on the boundary portion that is not shared with any other domain, E_i, and the sets of points shared with other domains, $S_{ii'}$. The continuity conditions on the shared boundaries and the external boundary conditions are given by

$$\left.\begin{aligned}
&\Phi_j^{(i)} = \Phi_{j'}^{(i')}\\
&D_j^{(i)} = D_{j'}^{(i')}
\end{aligned}\right\} \ \forall j, j' : j \in S_{ii'}, j' \in S_{i'i},$$
$$\Phi_j^{(i)} = \Phi_{0j}^{(i)} \quad \forall j \in E_i, \tag{A2}$$

where $\Phi_{0j}^{(i)}$ is the electrostatic potential on the external boundary of subdomain i. The set of Eqs. (A1) combined with the boundary conditions leads to the following general expression

$$\begin{aligned}
&\sum_{j'\in E_i} G_{jj'}^{(i)} D_{j'}^{(i)} + \sum_{i'=1;i'\neq i}^{N}\left\{\sum_{j'\in S_{ii'}}[G_{jj'}^{(i)} D_{j'}^{(ii')} + G'^{(i)}_{jj'}\Phi_{jj'}^{(ii')}]\right.\\
&\left. + \delta_j^{S_{ii'}}\Phi_j^{(ii')}\right\} = -\delta_j^{E_i}\Phi_{0j}^{(i)} - \sum_{j'\in E_i} G'^{(i)}_{jj'}\Phi_{0j'}^{(i)},
\end{aligned} \tag{A3}$$

where $D_j^{(ii')}$ and $\Phi_j^{(ii')}$ are the fields on the shared boundaries and

$$\delta_i^S = \begin{cases} 1 & \text{if} \quad i \in S\\ 0 & \text{otherwise.}\end{cases} \tag{A4}$$

The solution to this set of equations gives the electrostatic potential on the shared boundaries and the electric field on the shared boundary and the external boundary.

APPENDIX B

The transmission coefficient through the 1D potential barrier is calculated by using the transfer matrix technique combined with the Runge–Kutta method of order four. The

starting differential equations for the wave function and its derivative are derived from the Schrödinger equation and are given as follows:

$$\begin{aligned}&\partial_x\psi=\psi',\\&\partial_x\psi'=\alpha(V(x)-E)\psi,\\&\alpha=\frac{2m}{\hbar^2},\end{aligned}\tag{B1}$$

where $V(x)$ describes the potential barrier and E is the incident electron energy. The transfer matrix method relates the wave function and its derivative before and after the barrier in the following manner:

$$\begin{pmatrix}\psi(x_N)\\ \psi'(x_N)\end{pmatrix}=M\begin{pmatrix}\psi(x_0)\\ \psi'(x_0)\end{pmatrix},\tag{B2}$$

where M is the transfer matrix. We choose x_0 and x_N smaller and larger than the smallest and largest classical turning points, respectively, such that the potential is well described by a constant at x_0 and by the linear electrostatic potential at x_N. After dividing the segment $[x_0,x_N]$ into equal intervals of length h, the Runge–Kutta method gives the following expression for the transfer matrix:

$$M=\prod_{i=1}^{N}M_i,\tag{B3}$$

where the four components of M_i, the transfer matrix for each interval, are

$$\begin{aligned}M_i(1,1)&=1+\frac{h^2}{6}\alpha(V_i-E)+\frac{h^2}{3}\alpha(V_{i+1/2}-E)\\&\quad+\frac{h^4}{24}\alpha^2(V_{i+1/2}-E)(V_i-E),\\M_i(1,2)&=h\left[1+\frac{h^2}{6}\alpha(V_{i+1/2}-E)\right],\\M_i(2,1)&=\frac{h}{3}\left[\frac{\alpha}{2}(V_i-E)+2\alpha(V_{i+1/2}-E)+\frac{\alpha}{2}(V_{i+1}\right.\\&\quad\left.-E)+\frac{h^2}{4}\alpha^2(V_{i+1/2}-E)(V_i+V_{i+1}-2E)\right],\\M_i(2,2)&=1+\frac{h^2}{3}\alpha(V_{i+1/2}-E)+\frac{h^2}{6}\alpha(V_{i+1}-E)\\&\quad+\frac{h^2}{24}\alpha^2(V_{i+1/2}-E)(V_{i+1}-E).\end{aligned}\tag{B4}$$

The wave function and its derivative before the barrier are given by the superposition of the forward propagating incident wave and the backward propagating reflected wave and can be written as follows:

$$\begin{aligned}\psi(x_0)&=C_{PW}(e^{ik_0x_0}+A_Re^{-ik_0x_0}),\\\psi'(x_0)&=C_{PW}ik_0(e^{ik_0x_0}-A_Re^{-ik_0x_0}),\end{aligned}\tag{B5}$$

where A_R is the reflection amplitude and C_{PW} is a normalization constant (see later). After the barrier, the transmitted wave is described by the forward propagating eigenstate of the Schrödinger equation with a linear potential. In order to find this solution we use the stationary eigenstate ψ_S, which is proportional to an Airy function Ai[13]

$$\begin{aligned}&\psi_S(x_N)=C_AA_TAi[-\xi(x_N)],\\&\xi(x)=\left(\frac{2meF}{\hbar^2}\right)^{1/3}\left(x-\frac{W-E}{eF}\right),\\&Ai(x)=\frac{\sqrt{\pi|x|}}{3}\{J_{-1/3}[u(x)]+J_{1/3}[u(x)]\},\quad x<0,\\&u(x)=\tfrac{2}{3}|x|^{3/2},\end{aligned}\tag{B6}$$

$$u(x)=\tfrac{2}{3}|x|^{3/2},\tag{B7}$$

where A_T is the transmission amplitude and C_A is a normalization constant (see later). The Bessel functions $J_{\pm1/3}$ can be expressed as sums of forward and backward propagating Hankel functions[14]

$$J_{\pm1/3}(x)=\tfrac{1}{2}[H^{(1)}_{\pm1/3}(x)+H^{(2)}_{\pm1/3}(x)].\tag{B8}$$

The forward propagating eigenstate of the Schrödinger equation with a linear potential and its derivative are thereby given by the following expressions:

$$\begin{aligned}\psi(x_N)&=\frac{C_A}{\sqrt{2}}A_T\frac{\sqrt{\pi|x_N|}}{3}[H^{(1)}_{-1/3}(u)+H^{(1)}_{1/3}(u)],\\\psi'(x_N)&=-\frac{C_A}{\sqrt{2}}A_T\frac{\sqrt{\pi}}{3}\left\{\frac{H^{(1)}_{-1/3}(u)+H^{(1)}_{1/3}(u)}{2\sqrt{|x_N|}}\right.\\&\quad\left.+|x_N|[H'^{(1)}_{-1/3}(u)+H'^{(1)}_{1/3}(u)]\right\},\end{aligned}\tag{B9}$$

$$u=\tfrac{2}{3}|\xi(x_N)|^{3/2}.\tag{B10}$$

The normalization constants for both the plane wave and the Airy function are chosen such that

$$\int_{-\infty}^{\infty}\psi_E^*(x)\psi_{E'}(x)dx=\delta(E-E'),\tag{B11}$$

and are given by the following expressions:

$$\begin{aligned}C_{PW}&=\left\{\frac{m}{8\pi^2\hbar^2[E-V(x_0)]}\right\}^{1/4}\\C_A&=\frac{(2m)^{1/3}}{\sqrt{\pi}\hbar^{2/3}(eF)^{1/6}}.\end{aligned}\tag{B12}$$

By using the transfer matrix equation we can calculate the coefficients A_R and A_T

$$\begin{aligned}&A_T=\frac{\Delta_1}{\Delta},\quad A_R=\frac{\Delta_2}{\Delta},\\&\Delta=\phi_NC_{PW}(ik_0M_{22}-M_{21})-\phi'_NC_{PW}(ik_0M_{12}-M_{11}),\\&\Delta_1=2ik_0\det(M)C^2_{PW},\\&\Delta_2=\phi_NC_{PW}(ik_0M_{22}+M_{21})-\phi'_NC_{PW}(ik_0M_{12}+M_{11}),\end{aligned}\tag{B13}$$

$$\phi_N = \frac{\psi(x_N - x_0)}{A_T}, \quad \phi'_N = \frac{\psi'(x_N - x_0)}{A_T}. \tag{B14}$$

In order to avoid roundoff errors, we found that it is important to calculate the determinant of the transfer matrix by using the matrix multiplication rule

$$\det(M) = \prod_{i=1}^{N} \det(M_i). \tag{B15}$$

The transmission (reflection) coefficient is given by the ratio of the transmitted (reflected) to the incident current probability

$$T = \frac{J(x_N)}{J(x_0)},$$

$$R = |A_R|^2, \tag{B16}$$

$$J(x) = \frac{\hbar}{2mi}[\psi^*(x)\psi'(x) - \psi(x)\psi'^*(x)]. \tag{B17}$$

[1] P. A. Knipp and T. L. Reinecke, Phys. Rev. B **54**, 1880 (1996).
[2] R. L. Hartman, W. A. Mackie, and P. R. Davis, J. Vac. Sci. Technol. B **12**, 754 (1994).
[3] A. A. Lucas, H. Morawitz, G. R. Henry, J.-P. Vigneron, Ph. Lambin, P. H. Cutler, and T. E. Feuchtwang, Phys. Rev. B **37**, 10708 (1988).
[4] W. H. Press, S. A. Teukolsky, W. T. Vetterling, and B. P. Flannery, *Numerical Recipes in C* (Cambridge University Press, New York, 1992).
[5] H. G. Kosmahl, IEEE Trans. Electron Devices **38**, 1534 (1991).
[6] A. Modinos, *Field, Thermionic, and Secondary Electron Emission Spectroscopy* (Plenum, New York, 1984).
[7] J. L. Shaw, Proceedings of the Materials Research Society Meeting, San Francisco, 1999 (unpublished).
[8] G. N. Fursey and D. V. Glazanov, J. Vac. Sci. Technol. B **16**, 910 (1998).
[9] P. H. Cutler, J. He, J. Miller, N. M. Miskovsky, B. Weiss, and T. E. Sullivan, Prog. Surf. Sci. **42**, 169 (1993).
[10] A. Mayer and J.-P. Vigneron, Phys. Rev. B **56**, 12599 (1997).
[11] Z. W. Huang, T. E. Feuchtwang, P. H. Cutler, and E. Kazes, Phys. Rev. A **41**, 32 (1990); J. L. Gervais, Phys. Rev. D **16**, 3507 (1977); T. Banks, C. M. Bender, and T. T. Wu, *ibid.* **8**, 3346 (1973).
[12] B. R. Chalamala, Y. Wei, and B. E. Gnade, IEEE Spectr. **35**, 42 (1998).
[13] L. Landau and E. Lifshitz, *Quantum Mechanics* (Butterworth, Washington, DC, 1997).
[14] Geroge Arfken, *Mathematical Methods for Physicists* (Academic, New York, 1985).